Contents lists available at ScienceDirect

Applied Catalysis B: Environmental

Novel MnS/(In$_x$Cu$_{1-x}$)$_2$S$_3$ composite for robust solar hydrogen sulphide splitting via the synergy of solid solution and heterojunction

Meng Dan[a,b], Shiqian Wei[b], Dmitry E. Doronkin[c], Yi Li[b], Ziyan Zhao[b], Shan Yu[b], Jan-Dierk Grunwaldt[c], Yuanhua Lin[a,b], Ying Zhou[a,b,*]

[a] *State Key Laboratory of Oil and Gas Reservoir Geology and Exploitation, Southwest Petroleum University, Chengdu 610500, China*
[b] *The Center of New Energy Materials and Technology, School of Materials Science and Engineering, Southwest Petroleum University, Chengdu 610500, China*
[c] *Insititue for Chemical Technology and Polymer Chemistry and Institute of Catalysis Research and Technology, Karlsruhe Institute of Technology, 76131 Karlsruhe, Germany*

ARTICLE INFO

ABSTRACT

Large photocatalytic hydrogen (H$_2$) production from copious waste hydrogen sulphide (H$_2$S) can meet the increasing demand for H$_2$ in a sustainable manor which is beneficial from both environmental and energy standpoints. In this work, we reported a robust MnS/(In$_x$Cu$_{1-x}$)$_2$S$_3$ composite photocatalyst. Both experimental results and density functional theory (DFT) calculations proved that Cu does not act as a cocatalyst but forms a solid solution ((In$_x$Cu$_{1-x}$)$_2$S$_3$) in the composites, which plays dual roles in improving the photocatalytic performance of H$_2$S splitting: (i) enhancing solar light absorption, and (ii) promoting the desorption of sulfur (S) adsorbed on the catalyst surface. Moreover, the formation of a heterojunction between γ-MnS and (In$_x$Cu$_{1-x}$)$_2$S$_3$ can significantly improve charge separation and migration in the composites. As a result, the MnS/(In$_x$Cu$_{1-x}$)$_2$S$_3$ exhibits greatly extended visible light absorption up to 599 nm and extraordinarily high photocatalytic H$_2$ production under visible light from H$_2$S with a maximum rate of 29,252 μmol h^{-1} g^{-1}. The corresponding apparent quantum efficiencies (AQE) at 420 and 450 nm are as high as 65.2% and 62.6%, respectively. They are the highest so far for the visible light photocatalytic splitting of H$_2$S in the absence of noble-metal co-catalysts.

1. Introduction

High-quality oil and natural gas reservoirs have been excessively used and depleted. Meanwhile, the energy consumption increased remarkably over the past years. To satisfy the fast growing energy demands, the oil and gas developments have to turn to high acid oil and gas reservoirs, in which hydrogen sulphide (H$_2$S) is an important component [1–3]. Every year, millions of tons ($> 4 \times 10^7$ t) of H$_2$S are produced around the world from oil-refinery plants and natural-gas extraction, and this trend will increase further in the future [4]. H$_2$S, owing to the extremely toxic, malodorous and corrosive nature, is a huge obstacle for exploiting acid oil and gas reservoirs. Hence, the effective removal of H$_2$S is highly desired. Most of the current industrial technology for removing H$_2$S is the Claus process [5], which is not an eco-friendly strategy because of the high temperature (ca. 1200 ℃) involved. Meanwhile, this process results in further environmental problems due to the generation of hazardous by-products, e.g. SO$_x$. More importantly, instead of capturing hydrogen (H$_2$) from H$_2$S, the Claus process ends up converting it to sulfur (S) and H$_2$O [6]. As a clean

energy carrier, H$_2$ has the highest energy density (120–142 MJ/kg) in comparison to any other fuels without carbon trace [7–10]. Therefore, the production of H$_2$ from H$_2$S is beneficial for both the abatement of the toxic pollutant and producing clean energy.

Over the past years, various strategies have been proposed for converting H$_2$S to H$_2$ and S [1]. Among them, the photocatalytic method, which can directly utilize abundant solar energy, has attracted considerable attention [11–15]. Nevertheless, the quest for suitable photocatalysts for H$_2$ production from H$_2$S is still a tremendous challenge as the catalyst deactivation was commonly observed during H$_2$S splitting process [16]. Recently, metal sulfides have been explored and verified to be more suitable photocatalysts compared to oxides for splitting H$_2$S as metal sulfides are more stable in the S-containing medium and can effectively reduce the catalyst deactivation [11,12,17–20]. Moreover, the serious photocorrosion of metal sulfides could be inhibited during photocatalytic splitting of H$_2$S process, because the photo-generated hole can be consumed by the excess of H$_2$S (H$_2$S + 2 h$^+$ → S + 2H$^+$) [17]. Unfortunately, single-phase metal sulfides usually suffer from low photocatalytic efficiency due to the

poor solar light absorption and fast recombination rate of photo-induced excitons [12,21–24]. To overcome these drawbacks, guiding the rational design of suitable photocatalysts to establish an efficient pathway to improve the efficiency of H_2 evolution from H_2S is essential.

To date, fabrication of heterojunction with other semiconductors was frequently used to effectively inhibit the electron-hole recombination [22–24], Numerous metal sulfide heterojunctions, such as $In_2S_3/MoS_2/CdS$ [25], $CuS@CuInS_2:In_2S_3$ [26], and $CdS/PANI$ [27], etc. have been reported for highly efficiency photocatalytic H_2 production due to their remarkable charge-separation and transfer efficiency. For instance, we previously reported an efficient MnS/In_2S_3 heterostructure photocatalyst with an apparent quantum yield (AQE) of 34.2% at 450 nm [17]. However, the light absorption ability of semiconductor heterojunctions was limited by the band gap position of the original single-phase photocatalyst. On the other hand, the formation of solid solution has been proposed as an elegant strategy to extend visible light absorption [28–31]. Among them, solid solutions containing copper have became a research hotspot. Akihiko Kudo et al. has reported a series of solid solutions containing copper with remarkable solar light absorption ability, such as $ZnS-CuInS_2-AgInS_2$ [28,29], $(CuIn)_xZn_{2(1-x)}S_2$ [30], $(CuGa)_{1-x}Zn_xS_2$ [31]. The density functional theory (DFT) calculations revealed that the contribution of Cu 3d orbital to the valence band is crucial to realize the superior visible-light-response. Therefore, the synergy of solid solution and heterojunction could offer a highly active visible light photocatalyst for H_2 production from H_2S. In addition, the formed S during the photocatalytic reaction can be adsorbed on the catalyst surface to block active sites [12,17]. Hence, the desorption ability of S on the catalyst surface is also crucial for long-term photocatalytic H_2 production from H_2S. To the best of our knowledge, most of the previous work only focused on one or two above aspects to enhance the photocatalytic performance, but very few non-noble metal photocatalysts can meet these strict demands.

In this work, a series of novel $MnS/(In_xCu_{1-x})_2S_3$ composites with hierarchical porous structures were successfully fabricated via a facile one-pot solvothermal method. They exhibit greatly extended light absorption up to 599 nm and outstanding visible light photocatalytic H_2 production from H_2S with a maximum H_2 production rate of 29,252 μmol h^{-1} g^{-1}. The corresponding AQE at 420 and 450 nm are as high as 65.2% and 62.6%, respectively. The local structure of Cu is identified through the combination of synchrotron-based experimental study and DFT calculations. Notably, CuS is not the active phase, instead, Cu is incorporated in the crystal structure of β-In_2S_3 to form $(In_xCu_{1-x})_2S_3$ solid solution, which can enhance the visible light absorption and promote the desorption of S adsorbed on the catalyst surface. Moreover, the formation of heterojunction between γ-MnS and $(In_xCu_{1-x})_2S_3$ can further improve charge separation and migration in the composites. These findings provide a new strategy for the design of robust photocatalysts for H_2S splitting via the synergy of solid solution and heterojunction.

2. Experimental section

2.1. Synthesis of the composites

In a typical procedure, $Mn(Ac)_2\cdot4H_2O$ (1.4 mmol), $InCl_3$ (0.6 mmol) and thioacetamide (TAA) (9.0 mmol) were dissolved in 23.8 mL pyridine (V_{Py}) to form a homogeneous solution. Subsequently, 1.2 mL of 0.05 M $Cu(Ac)_2\cdot H_2O$/pyridine ($V_{Cu/Py}$) solution was added dropwise in the above solution under constant stirring. The obtained solution was immediately transferred to a 50 mL Teflon-lined stainless steel autoclave and maintained at 180 °C for 30 h. After cooling to room temperature, the prepared precipitates were centrifuged and washed several times with ethanol. Finally, the powders were dried at 50 °C for 10 h. Similarly, other samples were synthesized under the same conditions, except for the values of V_{Py} and $V_{Cu/Py}$ (V_{Py} + $V_{Cu/Py}$ = 25 mL). The samples obtained with 0, 0.6, 1.2, 1.8, and 3.0 mL of $V_{Cu/Py}$ were

denoted as MnS/In_2S_3, MIC0.6, MIC1.2, MIC1.8 and MIC3.0, respectively. For comparison, MnS, In_2S_3, CuS, MnS/CuS and In_2S_3/CuS samples were also prepared under similar conditions.

2.2. Characterization

X-ray diffraction (XRD, PANalytical X'pert with Cu Kα radiation) was performed to investigate the structure and crystallinity. Inductively coupled plasma atomic emission spectrometry (ICP, Varian ES) was used to identify the compositions of these samples. Scanning electron microscopy (SEM, JEOL JSM-7800 F) and Transmission electron microscopy (TEM, Tecnai G2 F30) were used to investigate the morphology and microstructure. Energy dispersive X-ray spectroscopy (EDX) was used to obtain elemental mapping. X-ray photoelectron spectroscopy (XPS, Thermo ESCALAB250Xi) measurements were performed to investigate the surface chemical composition and binding environment of samples and all of the binding energies were referenced to the C 1 s level at 284.8 eV. UV–vis diffuse reflectance spectra (DRS, Shimadzu UV-2600) were recorded at room temperature with an integrating sphere using Ba_2SO_4 as the reflectance standard. The N_2 adsorption-desorption isotherm and pore-size distributions were determined by the nitrogen adsorption method (Quadrasorb SI), the specific area of the samples was calculated using the Brunauer-Emmett-Teller (BET) method [32]. The samples were degassed at 110 °C for 8 h under vacuum before measurements.

X-ray absorption spectra in terms of X-ray Absorption Near Edge Structure (XANES) and Extended X-ray Absorption Fine Structure (EXAFS) were measured at the CAT end station of the CAT-ACT beamline at the Synchrotron Radiation Source at KIT, Karlsruhe [33]. The samples were measured *ex situ* at Cu K absorption edge in transmission mode in form of pellets prepared with cellulose. The beam size was 0.5 mm (vertical) x 1 mm (horizontal). The spectra were normalized and the EXAFS background subtracted using the ATHENA program from the IFFEFIT software package [34]. Linear combination analysis of the MIC3.0 sample spectrum was performed using ATHENA in the energy range 8973–9013 eV. The structure refinement was performed using ARTEMIS software (IFFEFIT) [35]. For this purpose, the corresponding theoretical backscattering amplitudes and phases were calculated and then adjusted to the experimental spectra by a least square method in R space between 1.0 and 2.5 Å (k range 3.0–10.7 Å^{-1}). First, the amplitude reduction factor (S_0^2 = 0.88) was calculated using the CuS reference spectrum, and then the coordination numbers (CN), interatomic distances (d), energy shift (ΔE_0) and mean square deviation of interatomic distances (σ^2) were refined. The absolute misfit between theory and experiment was expressed by ρ.

XANES spectra were modeled using multiple scattering FEFF 9.6.4. *ab initio* code [36]. For the CuS spectrum two calculations were done using CuS model structure (ICSD collection code 41,911) and calculating spectra for both inequivalent Cu sites, the spectra were then averaged taking into account the corresponding multiplicities. Radius of the clusters for self-consistent potential calculations (SCF) and for full multiple scattering calculations (FMS) was set as 5 Å.

2.3. DFT calculation

The density functional theory (DFT) calculations were performed using the generalized gradient approximation (GGA) exchange-correlation functional of the Perdew-Burke-Ernzerhof (PBE) type [37] as implemented in the Vienna ab initio simulation package (VASP) [37]. The cut-off energy of the plane-wave expansion was set to 300 eV. All geometries were adequately optimized until the convergence criteria of energy and force reached 2×10^{-4} eV and 0.02 eV/Å, respectively. The Brillouin zone was sampled with $2 \times 2 \times 1$, $2 \times 2 \times 2$ and $2 \times 1 \times 1$ Monkhorst-Pack k-point grids for the structure optimizations and total energy calculations of the γ-MnS (P63mc) bulk, β-In_2S_3 (Fd-3m:2) bulk and β-In_2S_3 (440) surface, respectively.

2.4. Photocatalytic tests

Photocatalytic H_2S splitting was carried out in a home-made photoreactor (50 mL Pyrex flask). As shown in Fig. S13, it contains three parts: H_2S generation (I), photocleavage of H_2S (II), and tail-gas unit (III). Powder samples (2.5 mg) were suspended in an aqueous solution (50 mL) containing Na_2S (0.1 mol L^{-1}) and Na_2SO_3 (0.6 mol L^{-1}) under magnetic stirring. Then, the home-made system was purged with Ar for 30 min to remove O_2 and CO_2 dissolved in aqueous solution followed by bubbling 3 M H_2S in the solution for 3 h at room temperature. Finally, the reactor was irradiated with a 300 W Xe lamp with a cutoff filter ($\lambda > 420$ nm). The amount of generated H_2 was monitored via a Shimadzu GC-2010 Plus gas chromatograph (GC, Ar carrier gas, molecular sieve 5 Å, TCD detector). The H_2 evolution rates were calculated based on H_2 amount generated in the first 6 h of reaction.

2.5. The apparent quantum efficiency (AQE)

The apparent quantum yield (AQE) was calculated according to Eq. (1). The number of evolved H_2 molecules was measured by GC (Shimadzu GC-2010 Plus) and the number of incident photons was determined from the output of a monochromatic LED lamp.

$$\begin{aligned} AQE(\%) &= \frac{\text{number of reacted electrons}}{\text{number of incident photos}} \times 100 \\ &= \frac{2 \times \text{number of evolved } H_2 \text{ molecules}}{\text{number of incident photons}} \times 100 \end{aligned} \quad (1)$$

2.6. Photoelectrochemical Measurements

The CHI660E electrochemical workstation (Chenhua Instrument, Shanghai, China) with a standard three-electrode system was used to investigate the photoeletrochemical properties of all the samples in a quartz cell. The cleaned ITO glass deposited with samples, a Pt foil and saturated calomel electrode (SCE) were used as working electrodes, counter electrode, and the reference electrode, respectively. 1.2 M Na_2SO_3 was used as electrolyte. The photocurrent measurements and electrochemical impedance spectroscopy over all the samples at open circuit potential were tested under visible-light irradiation ($\lambda > 420$ nm).

3. Results and discussion

The photocatalytic performance of all the as-obtained samples was evaluated by H_2 production from H_2S under visible-light irradiation ($\lambda > 420$ nm). The samples synthesized at 180 °C for 30 h with different compositions were denoted as MIC0.6, MIC1.2, MIC1.8, and MIC3.0, using an increasing volume of 0.05 M $Cu(CH_3COO)_2 \cdot H_2O$ precursor as described in the Experimental section. The blank experiments revealed that H_2 was not detected in the absence of photocatalyst or light irradiation. As shown in Fig. 1a and b, the addition of Cu in the composites can enhance the photocatalytic activity in general and the photocatalytic performance strongly depends on the Cu content in the composites. The photocatalytic H_2 evolution rate gradually increased with increasing the amount of Cu. The MIC1.2 sample reveals the highest photocatalytic activity with H_2 evolution rate of 29,252 μmol $h^{-1} g^{-1}$, which was ca. 2.5 times higher than that of the pristine MnS/In$_2$S$_3$ (11,945 μmol $h^{-1} g^{-1}$) and 1400 times higher than that of CuS (21 μmol $h^{-1} g^{-1}$) alone. Meanwhile, a significant amount of bubbles were observed over MIC1.2 during the photocatalytic H_2S splitting process (Movie S1), confirming the boost of the photocatalytic H_2 production. With further increasing the amount of Cu in the composites, the compositions are unfavorable for the splitting of H_2S. Notably, the H_2 evolution rate of MIC3.0 (10,348 μmol $h^{-1} g^{-1}$) is even lower than that of the pristine MnS/In$_2$S$_3$ (11,945 μmol $h^{-1} g^{-1}$). Besides, stability is also crucial for the evaluation of photocatalytic

performances. Hence, the stability of the MIC1.2 sample was examined by repeating the experiment for 5 times (Fig. 1c). No decrease of the activity was observed, confirming that the MIC1.2 sample has an excellent stability. Further investigation was performed to explore the stability of MIC1.2 sample. First, the XRD patterns of MIC1.2 sample after the photocatalytic H_2 evolution reaction was shown in Fig. S1a, in which no distinguishable change can be observed, confirming that the MIC1.2 photocatalysts has good durability in the photocatalytic H_2S splitting reaction process. Meanwhile, the XPS measurement was also conducted to study the surface chemical composition and binding environment of MIC1.2 after reaction, as shown in Fig. S1b-f. The result showed that the binding energy of Mn 2p, In 3d, Cu 2p, and S 2p for the MIC1.2 sample after reaction was also not changed as compared with MIC1.2 sample before reaction (Fig. S6). Thus, these results indicate that the MnS/(In$_x$Cu$_{1-x}$)$_2$S$_3$ composites possess superior photostability.

Fig. 1d shows the wavelength-dependent AQE of photocatalytic H_2 evolution from H_2S splitting over MIC1.2 together with its UV–vis diffuse reflectance spectra (UV–vis DRS). In fact, the H_2 production is wavelength dependent which is consistent with the UV–vis DRS and it confirms that the observed H_2 generation over MIC1.2 comes from a photocatalytic process [28]. The AQE at 420 nm and 450 nm are as high as 65.2% and 62.6%, respectively, which are, to our knowledge, the highest for the visible light photocatalytic splitting of H_2S in the absence of noble-metal co-catalysts (cf. Table S1 and Table S2). To investigate the role of each component in the composites on the photocatalytic activity, the photocatalytic performance of each component as well as the corresponding composites is shown in Fig. S2. By contrast, MnS (4 μmol $h^{-1} g^{-1}$), CuS (21 μmol $h^{-1} g^{-1}$), In$_2$S$_3$ (169 μmol $h^{-1} g^{-1}$), MnS/CuS (5 μmol $h^{-1} g^{-1}$), (In$_x$Cu$_{1-x}$)$_2$S$_3$ (6526 μmol $h^{-1} g^{-1}$) and MnS/In$_2$S$_3$ (11,945 μmol $h^{-1} g^{-1}$) exhibited much lower H_2 evolution rates compared to the MIC1.2 sample (29,252 μmol $h^{-1} g^{-1}$). These results clearly illustrate that Mn, In, and Cu are all indispensable for the MIC1.2 sample to achieve the highly efficient photocatalytic H_2S splitting.

Typically, a photocatalytic reaction process over semiconductors is determined by three factors: (i) solar light absorption ability, (ii) the efficiency of charge separation and migration and (iii) the catalytic reaction on surfaces [12,23,38]. Hence, firstly, the influence of the introduction of Cu in the composites on the solar light absorption ability was investigated by the UV–vis DRS. As shown in Fig. 2, MIC0.6, MIC1.2 and MIC1.8 possess steep absorption edges which extend to the visible region, indicating that the visible light absorption was due to a band transition instead of the formation of impurity levels. According to the onset of the absorption edge, the band gaps (E_g) of the pristine MnS/In$_2$S$_3$, MIC0.6, MIC1.2 and MIC1.8 were determined as 2.47, 2.15, 2.07 and 2.08 eV, respectively (Table S3). The corresponding colours changed from yellow to brown. It is worth noting that the MIC3.0 sample exhibits completely different behaviour. An additional absorption region ranging from 600 to 800 nm was observed for MIC3.0 [39], which could be attributed to the absorption of CuS (Fig. S3). In combination with the photocatalytic results of these samples (Fig. 1), it can be concluded that with increasing the amount of Cu in the composites CuS was formed which did not play a positive role as cocatalyst [40,41] but impaired the photocatalytic performance of the composites. In addition to the optical absorption, the edge positions are also very important for the photocatalytic reactions. The valence band (VB) positions of the pristine MnS/In$_2$S$_3$, MIC1.2 and MIC3.0 were determined to be 0.75, 0.35 and 0.58 eV by the valence-band XPS spectra (Fig. S4). Given that their band gaps are 2.47 (MnS/In$_2$S$_3$), 2.07 (MIC1.2) and 2.09 eV (MIC3.0), the corresponding conduction band (CB) positions are considered to be -1.72, -1.72 and -1.51 eV, respectively. These results confirm that all the samples possess suitable band gap structures for the photocatalytic H_2 evolution from H_2S.

Furthermore, we have carried out the transient photocurrent response and electrochemical impedance spectroscopy (EIS) to investigate the photo-generated charge carrier behaviours, as shown in
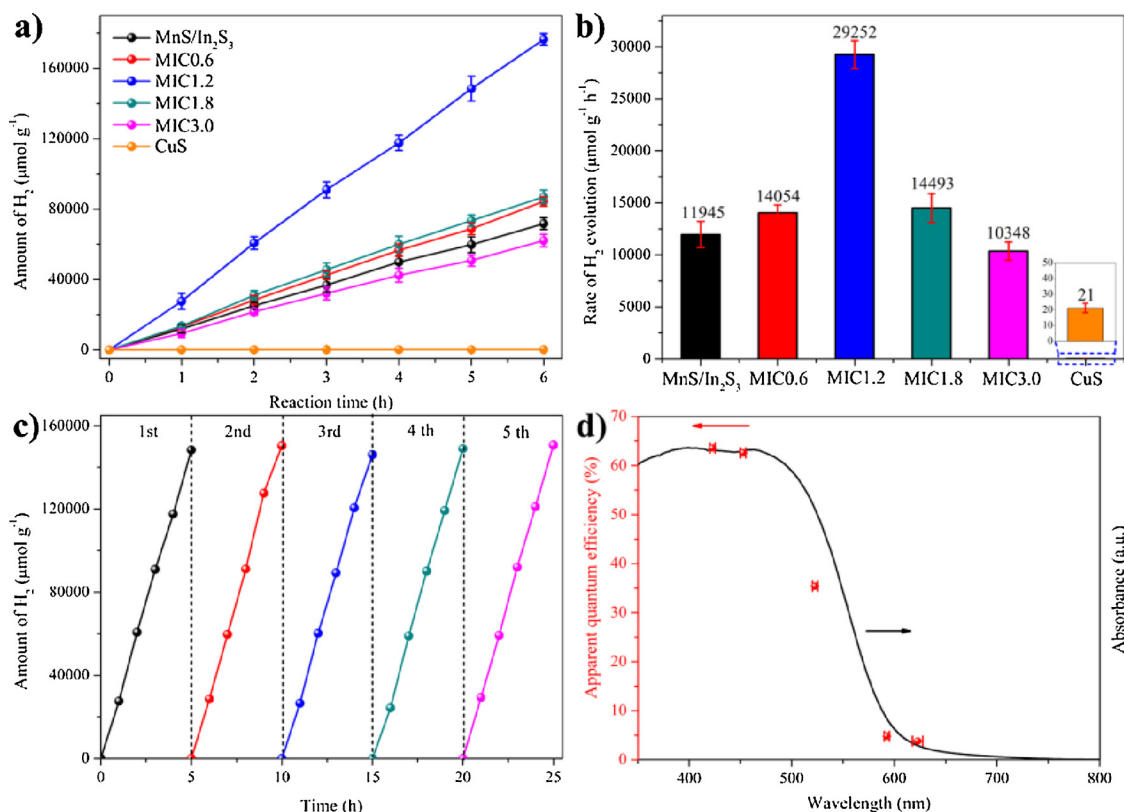
Fig. 1. a) Photocatalytic H_2 production over all tested samples under visible-light irradiation ($\lambda > 420$ nm); b) Comparison of the visible-light photocatalytic H_2 evolution rate over all samples; c, d) Cycling test and the wavelength-dependent quantum efficiency (QE) of photocatalytic H_2 evolution over MIC1.2 together with its UV–vis DRS. Reaction conditions: reaction solution, Na_2SO_3-Na_2S (0.6 mol/L-0.1 mol/L) aqueous solution (50 mL); concentration of H_2S, 3 M; catalyst loading, 0.0025 g; light source, 300 W Xe lamp with a cut off filter ($\lambda > 420$ nm); reaction cell, Pyrex.
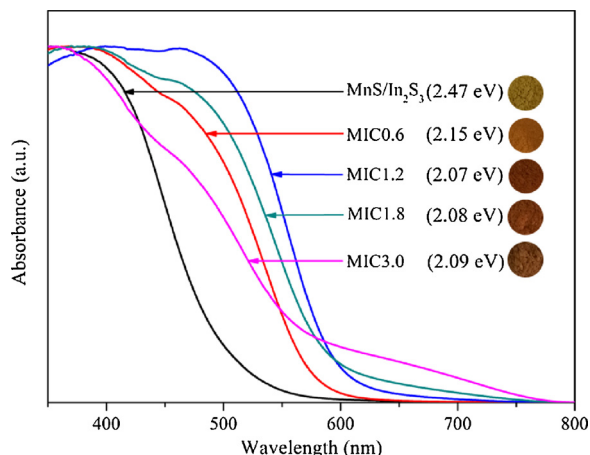

Fig. 2. UV–vis DRS of the prepared samples.

Fig. 3. In line with the photocatalytic activity (Fig. 1a and b), the Cu loaded samples exhibited an enhanced transient photocurrent response except for the MIC3.0 (Fig. 3a). Among them, the MIC1.2 sample shows the highest photocurrent, suggesting that the photo-generated electrons and holes can be efficiently separated. A similar result was found in the EIS test (Fig. 3b). The decreased arc radius of the Nyquist plot demonstrates a smaller charge transfer resistance. All in all, on the basis of the above results, it is obvious that the addition of Cu into MnS/In_2S_3 has a significant influence on the light absorption, band structure and charge separation process of MnS/In_2S_3 as well as the resulting photocatalytic performances. Notably, the loaded Cu could play a negative role once CuS is formed. Hence, it seems that the local structure of Cu

plays a crucial role, which has been further studied by various experimental methods and DFT calculations, as reported in the following sections.

First, the compositions of these samples were identified by the ICP elemental analysis (Table S4). With increasing amount of Cu $(CH_3COO)_2 \cdot H_2O$ precursor, the atomic fraction of Cu in the composites increased from 3.0% (MIC0.6) to 12.1% (MIC3.0), revealing that Cu was successfully introduced in all composites. Meanwhile, the atomic fraction of Mn in the composites decreased in two steps: from 51.3% (MnS/In_2S_3) to 48.6% (MIC1.2) and from 48.6% (MIC1.2) to 40.4% (MIC3.0). Thus, the significant decrease of the amount of Mn was observed once the Cu$(CH_3COO)_2 \cdot H_2O$ precursor amount exceeded 1.2 mL (MIC1.8 and MIC3.0), which can be attributed to the discrepancy of the solubility constants of the final products, corresponding to the solubility constants of $Ksp = 4.65 \times 10^{-14}$ and $Ksp = 6.3 \times 10^{-36}$ for MnS and CuS, respectively. [17,41] This result illustrates that the CuS phase could be formed in the MIC1.8 and MIC3.0 samples, because the crystallization of CuS occurs faster than MnS.

Then, XRD was performed to investigate the crystal structure of these samples (Fig. 4a). In the absence of Cu$(CH_3COO)_2 \cdot H_2O$ precursor, all diffraction peaks can be indexed into hexagonal γ-MnS (JCPDS 40–1289) and β-In_2S_3 (JCPDS 65-0459), which agrees well with the previous work [17]. Additionally, in the absence of $InCl_3$ and Mn $(CH_3COO)_2 \cdot 4H_2O$, the sample can be indexed to hexagonal CuS (JCPDS 06-0464), as shown in Fig. S5. With the addition of Cu precursor, all samples present a similar crystal structure, revealing that Cu^{2+} ions did not significantly change the crystal structure of the MnS/In_2S_3. Unexpectedly, no diffraction peaks of CuS or any other Cu contained phases were observed for MIC1.8 and MIC3.0. This indicated that the formed Cu contained species in these samples are either highly dispersed or amorphous. With further careful analysis of the XRD patterns,
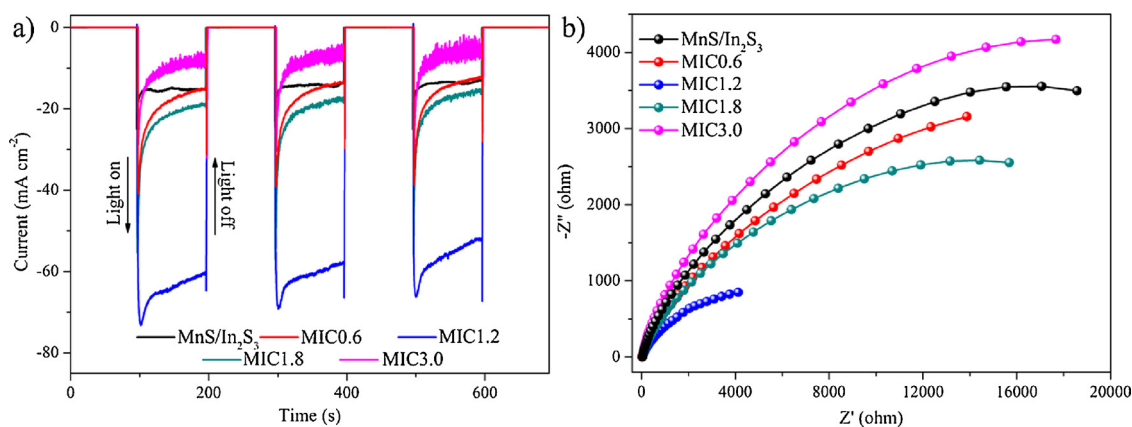
Fig. 3. a) Transient photocurrent response, b) EIS of all the prepared samples. Test conditions: The photoelectrochemical measurements over all the samples at open circuit potential were tested under visible-light irradiation ($\lambda > 420$ nm), the 1.2 M Na_2SO_3 solution as electrolyte.

it is worth noting that the diffraction peaks (e.g. the (440) plane of β-In_2S_3) shifted to higher angles after the introduction of Cu (from 46.905° to 47.091°) (Fig. 4b). This phenomenon could be attributed to the fact that Cu^{2+} (0.74 Å) may prefer to replace In^{3+} (0.76 Å) to form $(In_xCu_{1-x})_2S_3$ solid solution rather than Mn^{2+} in MnS as the ionic radius of Cu^{2+} (0.74 Å) is much larger than that of Mn^{2+} (0.46 Å) [27,42,43]. Hence, the diffraction peaks of β-In_2S_3 shifted slightly to higher angles. Among these samples, the MIC1.2 has a maximum peak shift of 0.186° (Fig. 4b). These results revealed that the formation window of $(In_xCu_{1-x})_2S_3$ solid solution is relatively narrow. With the excess of Cu precursor, other Cu-containing species, such as CuS, could be formed and the formation of $(In_xCu_{1-x})_2S_3$ solid solution is inhibited.

In order to verify the above analysis, DFT calculations were performed to explore the state of Cu in the composites. The thermodynamic stability of Cu-doped γ-MnS and β-In_2S_3 were described by the formation energies (E_f). For example, the E_f of Cu-MnS was calculated by the following Eq. (2):

$$E_f = E_{Cu-MnS} - E_{Cu} - E_{MnS} + E_{Mn} \tag{2}$$

where E_{Cu-MnS}, E_{Cu}, E_{Mn} and E_{MnS} were the total energies of Cu-MnS, a Cu atom in bulk Cu, a Mn atom in bulk Mn and bulk MnS, respectively. As shown in Fig. 4c, the E_f of Cu-MnS and Cu-In_2S_3 are 6.96 eV and -1.67 eV, respectively, indicating that the Cu-In_2S_3 system is thermodynamically much more stable than Cu-MnS. Additionally, the lattice parameters of γ-MnS significantly changed once Cu is loaded in the γ-MnS, while the effect of loading Cu on the lattice parameters of β-In_2S_3 can be neglected (Table S5). Based on these results, it is obvious that the formation of $(In_xCu_{1-x})_2S_3$ solid solution is more preferred than Mn_xCu_{1-}
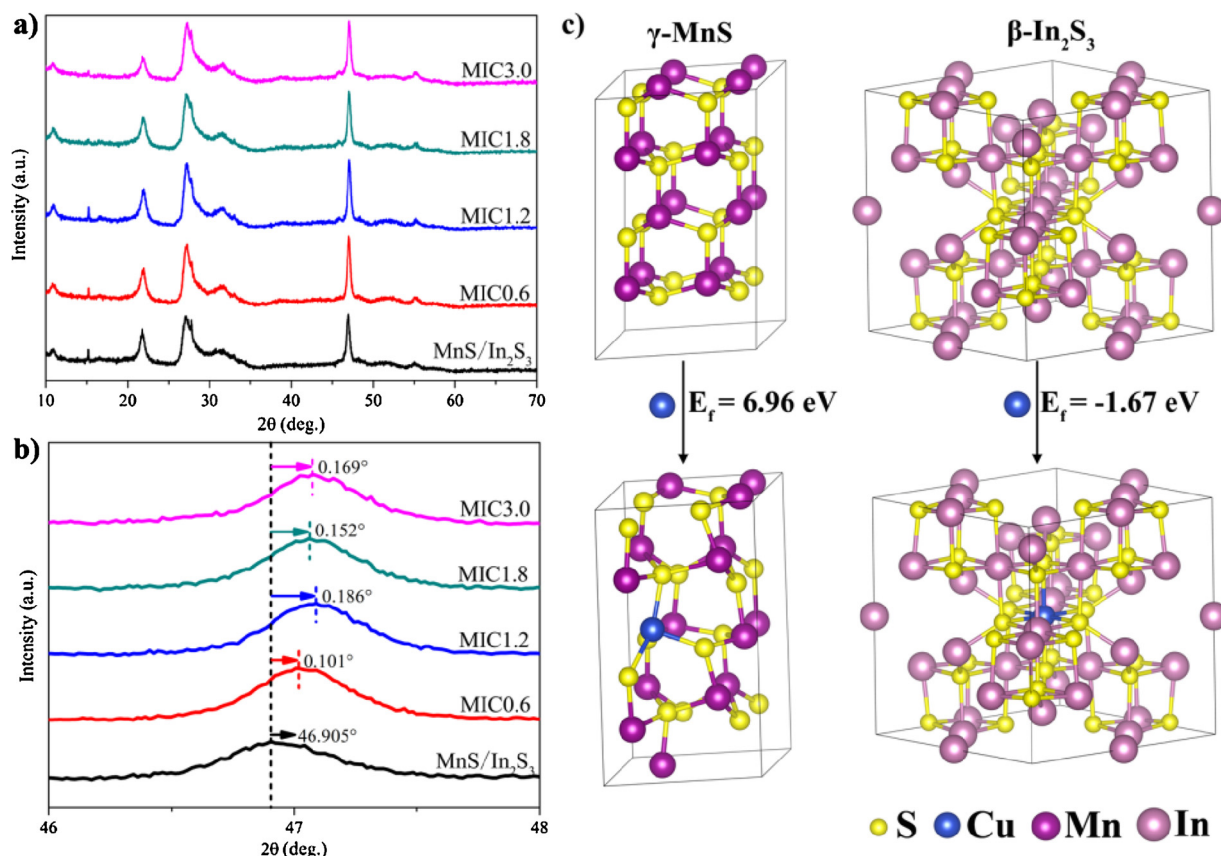

Fig. 4. a, b) XRD patterns of all the samples, c) The crystal structures of MnS and In_2S_3 before and after the introduction of Cu.

$_x$S when Cu is injected into the MnS/In$_2$S$_3$, which is in accordance with the result of XRD analysis.

The chemical state of the elements in MnS/In$_2$S$_3$, MIC1.2 and MIC3.0 were then investigated by X-ray photoelectron spectroscopy (XPS) (Fig. S6). Through the observation of high-resolution spectra of Mn 2p (Fig. S6b), In 3d (Fig. S6c), and S 2p (Fig. S6e) in MnS/In$_2$S$_3$, MIC1.2 and MIC3.0, it is found that they are almost the same, confirming the very similar nature of these elements in the composites. The high-resolution spectra of Mn 2p and In 3d can be ascribed to Mn^{2+} and In^{3+} in MnS/In$_2$S$_3$ composite [17]. The high-resolution spectra of S 2p can be attributed to S^{2-} in the sulphides [17]. Additionally, all the surface of these samples contains O element (Fig. S6f), which can be assigned to the surface adsorbed hydroxyl oxygen and water [17]. Notably, the main changes in the XPS spectra come in the Cu 2p XPS spectra (Fig. S6d). The binding energy of Cu 2p$_{1/2}$ and Cu 2p$_{3/2}$ for MIC3.0 is identified at 951.4 and 931.7 eV, which can be assigned to Cu^{2+} in CuS [44]. However, the two characteristic peaks at 951.5 and 932.1 eV in the spectra of MIC1.2 are ascribed to Cu 2p1/2 and Cu 2p3/2, which cannot be assigned to Cu^{2+} in CuS, because the separation of 19.4 eV does not correspond to that of the Cu 2p sates in CuS. Hence, the local structure of Cu in MIC1.2 is significantly different from that in MIC3.0 which demands further investigation.

For this purpose, XANES spectroscopy and EXAFS which enable the accurate determination of the chemical environment of a target element in a crystalline or amorphous matrix are very powerful. Here, the Cu K-edge XANES and EXAFS spectra were recorded in transmission mode at the CAT-ACT beamline at the Synchrotron Radiation Source at KIT, Karlsruhe. The spectra of all three samples are quite similar to each other and above the white line region (where EXAFS oscillation start) similar to a CuS spectrum (Figs. 5a and b). However, the orbital structures of composites (MIC0.6, MIC1.2 and MIC3.0) and CuS are quite different as seen in the region near the absorption edge in the Fig. 5b. When comparing the three composites, the spectra of MIC 1.2 and MIC 0.6 appear to be nearly identical whereas MIC3.0 is slightly different. X-ray absorption spectroscopy (XAS) is a bulk technique probing all atoms of a certain element in the sample, thus, in case of mixtures, an average spectrum is observed. Indeed, the XANES spectrum of MIC3.0 can be represented as a linear combination of spectra of MIC1.2 (93 ± 1%) and CuS (7 ± 1%) which proves that a mixture of different Cu species may be present in the MIC3.0. The EXAFS spectra of the composites (Fig. 5b) exhibit very similar oscillations to the CuS reference, although with a small shift. As a result, the Fourier-transformed EXAFS data (Fig. 5c) confirm that the first shells in CuS and composites (MIC0.6, MIC1.2 and MIC3.0) are nearly identical with similar number of S nearest neighbors. However, the average Cu-S distance in MnS/(In$_x$Cu$_{1-x}$)$_2$S$_3$ (MIC1.2) composites is 2.31 Å, longer than the 2.24 Å obtained for CuS, and suggests a different environment of Cu in MnS/(In$_x$Cu$_{1-x}$)$_2$S$_3$ (the results of EXAFS analysis are given in Table S6). Qualitatively, the conclusion of the different atomic environment around Cu is further supported by clearly different second shells (3–4 Å, Fig. 5c) in composites and CuS. The theoretical average number of S atoms in CuS is approx. 3.7 (resulting from averaging over two structurally independent Cu sites with different multiplicity in the hexagonal CuS structure), and the average number of S atoms around Cu in MnS/(In$_x$Cu$_{1-x}$)$_2$S$_3$ is 3.4 (Fig. 5c). This corresponds to a tetrahedral site, thus, Cu should displace In from tetrahedral sites in In$_2$S$_3$, which is in accordance with the calculated XANES spectra (Fig. S7). Furthermore, the Cu-S bond length of 2.31 ± 0.01 Å is smaller than typical In(tetr.)-S distance in In$_2$S$_3$ (2.47 Å, Table S6). This causes decreasing lattice constant which was observed as a shift of XRD reflections (Fig. 4).

Generally, photocatalytic reaction is a complex interplay of various factors such as crystal structure, surface area, partice size, morphology, interface and compositions. Hence, N$_2$ adsorption-desorption experiments were conducted to investigate the BET surface area and pore structure of these samples at 77.3 K. The N$_2$ adsorption/desorption isotherms of all samples are type IV (Fig. S8), which is characteristic of

mesoporous materials [45]. The shape of hysteresis loop is H3 type, implying that the formation of slit-like pores resulted from the aggregation of nanosheets [46,47]. The above results suggested that all samples have a hierarchical porous structure. The BET surface area, pore volume and average pore diameter of the samples were summarized in Table S7. All in all, the Cu contained composites (23-35 m^2 g^{-1}) exhibit a lower surface area compared to the pristine MnS/In$_2$S$_3$ (55 m^2 g^{-1}), indicating that the enhanced visible light photocatalytic activity after the introduction of Cu cannot be attributed to the enhancement of BET surface area.

SEM (Fig. 6) revealed that all the samples have a three-dimensional (3D) hierarchical morphology. The introduction of Cu did not change the inherent morphology of MnS/In$_2$S$_3$ as well. Nevertheless, it should be noticed that the surface roughness of the nanosheets was different from each other. With increasing amount of Cu(CH$_3$COO)$_2$·H$_2$O precursor, the surface of MIC1.8 and MIC3.0 samples became relatively rough with some particles on the top (Fig. 6d2 and e2). Through the combination of the results from UV–vis DRS (Fig. 2) and XAS (Fig. 5), these particles on the surface could be assigned to the low crystalline CuS species, which impaired the photocatalytic performance of the composites. Thus, we tried to remove these particles from the hierarchical structures over MIC3.0 by centrifugation. Fig. S9 shows SEM images of MIC3.0 before and after centrifugation. Although the particles could not be completely removed by centrifugation, the amount of particles on the surface obviously decreased. UV–vis DRS (Fig. S10a) further confirmed this phenomenon as the absorption in the visible light region ranging from 600 to 800 nm decreased accordingly. As a result, the H$_2$ evolution rate increased from 10,348 to 12,350 μmol h^{-1} g^{-1} (Fig. S10b).

TEM image (Fig. 7a and b) of MIC1.2 further confirmed the sheet-shaped building blocks and the hierarchical morphology. These nanosheets are mostly transparent under electron beam, revealing their ultrathin shape (ca. 12 nm). Fig. 7c and d shows the high-resolution TEM (HRTEM) image and the selected area electron diffraction (SAED) pattern of this sample. The (002) diffraction ring of γ-MnS and (440) plan of β-In$_2$S$_3$ (((In$_x$Cu$_{1-x}$)$_2$S$_3$)) clearly observed in SAED confirmed the existence of γ-MnS and β-In$_2$S$_3$ in MIC1.2. According to the HRTEM image, the β-In$_2$S$_3$ ((In$_x$Cu$_{1-x}$)$_2$S$_3$) nanosheets are in close contact with the γ-MnS to form layer heterostructures, which could play an important role on the transfer of photo-generated electrons and holes between γ-MnS and (In$_x$Cu$_{1-x}$)$_2$S$_3$ and suppresses their recombination as shown in Fig. 3. Moreover, the energy dispersive X-ray spectroscopy (EDX) mapping of MIC1.2 (Fig. 7e) confirmed that Mn, In, Cu, and S are uniformly distributed over the whole area of this sample. Fig. S11 shows the TEM, HRTEM, SAED and EDX mapping of MIC3.0. As a whole, this sample exhibited similar features with MIC1.2. Nevertheless, the major difference is that a Cu enrichment area in MIC3.0 (Fig. S11e) was observed, which further confirmed that CuS existed as a separate phase in this sample in accordance with the XAS analysis and SEM images.

On the basis of the above results, we found that MnS/(In$_x$Cu$_{1-x}$)$_2$S$_3$ composite is extraordinarily active for visible light photocatalytic H$_2$ production from H$_2$S. For water (H$_2$O) splitting, noble-metals were widely used as cocatalysts to realize high QE and photocatalytic activity. Unfortunately, they are easily deactivated in the presence of even small amounts of H$_2$S [48]. Therefore, the development of highly active noble-metal free photocatalysts for H$_2$S splitting with visible light response and long-term stability is essential. In our case, the preparation window of active MnS/(In$_x$Cu$_{1-x}$)$_2$S$_3$ composite is relatively narrow. With the excess amount of Cu precursor, low crystalline CuS is easily formed and impairs the photocatalytic activity significantly. The excellent performance of MnS/(In$_x$Cu$_{1-x}$)$_2$S$_3$ can be ascribed to the following reasons:

First, due to similar ionic radii of Cu^{2+} (0.74 Å) and In^{3+} (0.76 Å), the formation of (In$_x$Cu$_{1-x}$)$_2$S$_3$ solid solution is much more preferred than Mn$_x$Cu$_{1-x}$S. The formed (In$_x$Cu$_{1-x}$)$_2$S$_3$ can enhance the solar light
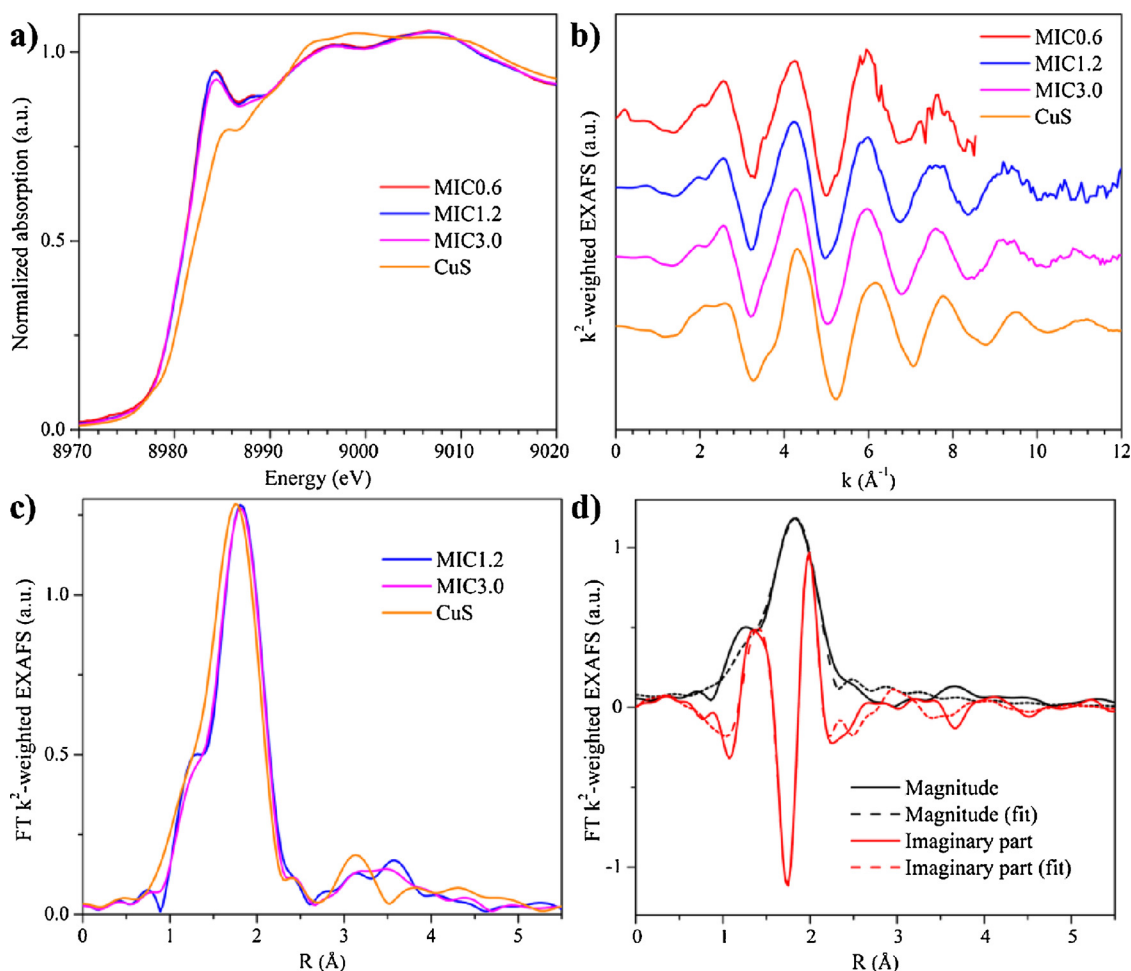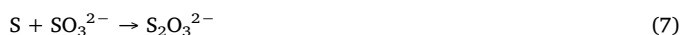
Fig. 5. a) XANES, b) k^2-weighted EXAFS, and c) Fourier-transformed (FT) k^2-weighted EXAFS spectra (in the k-range 2.3-10.7 Å^{-1}, uncorrected for the phase shift) of the MnS/$(In_xCu_{1-x})_2S_3$ composites with the CuS reference spectrum; d) fit of the EXAFS spectrum of the MIC1.2 sample.

absorption remarkably and extend visible light absorption up to 599 nm (cf. Fig. 2). In order to further explore the effect of incorporated Cu on the optical properties of β-In_2S_3, the dielectric functions of In_2S_3 and Cu-In_2S_3 were calculated based on the DFT calculation. It is found that the intensity of the peak at ca. 0.5 eV sharply increases after the introduction of Cu into the β-In_2S_3 (Fig. S12), indicating that the introduction of Cu promotes electron transfer from the VB to the CB under solar light irradiation. Therefore, the amount of photo-generated carriers in the $(In_xCu_{1-x})_2S_3$ is significantly higher than in the In_2S_3, which is beneficial to the photocatalyic activity.

Second, the desorption of S from the photocatalyst surface to bulk solution is crucial for the photocatalytic splitting of H_2S [12,17,18]. Compared to H_2O splitting, the photocatalytic oxidation products of splitting of H_2S are relatively complex. For instance, S^{2-} could be oxidized to S_n^{2-}, S, SO_2-, SO_4^{2-} and so on [49]. Hence, the long-term photocatalytic H_2 production from H_2S is even more challenging than from H_2O splitting as the photo-generated coloured S_n^{2-} could shield the light absorption [50] and S can be adsorbed on the catalyst surface and block the active sites. In this work, the 0.1 M Na_2S/0.6 Na_2SO_3 was used as reaction media for realizing the durable and high-efficiency photocatalytic H_2S splitting. Here, the 0.1 Na_2S/0.6 Na_2SO_3 plays three roles in improving the photocatalytic performance of H_2S splitting: (I) promoting the separation of photo-generated electrons and holes as electron donors (Eqs. (4), (5) and (8)), (II) improving the long-term stability of catalysts, because the addition of SO_3^{2-} can prevent the formation of yellow solid S or S_2^{2-} (Eqs. (6) and (7)), and (III) Providing sufficient HS- ions for the photocatalytic reaction as absorbent (Eq. (3)).

[17,18]

$$H_2S + OH^- \leftrightarrow HS^- + H_2O \tag{3}$$

$$2S^{2-} + 2h_{VB}^+ \rightarrow S_2^{2-} \tag{4}$$

$$HS^- + 2h_{VB}^+ \rightarrow H^+ + S \tag{5}$$

$$SO_3^{2-} + S_2^{2-} \rightarrow S_2O_3^{2-} + S^{2-} \tag{6}$$

$$S + SO_3^{2-} \rightarrow S_2O_3^{2-} \tag{7}$$

$$SO_3^{2-} + S^{2-} + 2h_{VB}^+ \rightarrow S_2O_3^{2-} \tag{8}$$

Indeed, the formed colourless $S_2O_3^{2-}$ favours the long-term H_2 production. However, the photocatalytic process still generate S which is hard to desorb from the surface of MnS/In_2S_3 [17,18]. Hence, it is necessary to investigate the S desorption on the MnS/$(In_xCu_{1-x})_2S_3$ composite. Moreover, considering the fact that photo-oxidation reaction (HS- + $2h_{VB}^+$ → H^+ + S) is occurring on β-In_2S_3 [17]. Therefore, the influence of the Cu-In_2S_3 on the S desorption performance was explored by DFT calculations, as shown in Fig. 8. The possibility of S desorption from surfaces was evaluated by the adsorption energy (E_{ads}) calculated using the Eq. (9):

$$E_{ads} = E_{adsorbate+slab} - E_{adsorbate} - E_{slab} \tag{9}$$

Where $E_{adsorbate+slab}$ and E_{slab} are the total energies of the substrate with and without the adsorbates respectively, and $E_{adsorbate}$ is the energy of adsorbed species. The more positive value of E_{ads} indicated that S desorption from the surface was much easier. The E_{ads} of S adsorbed on the surface of In_2S_3 and Cu-In_2S_3 are respectively -2.01 and -0.37 eV.
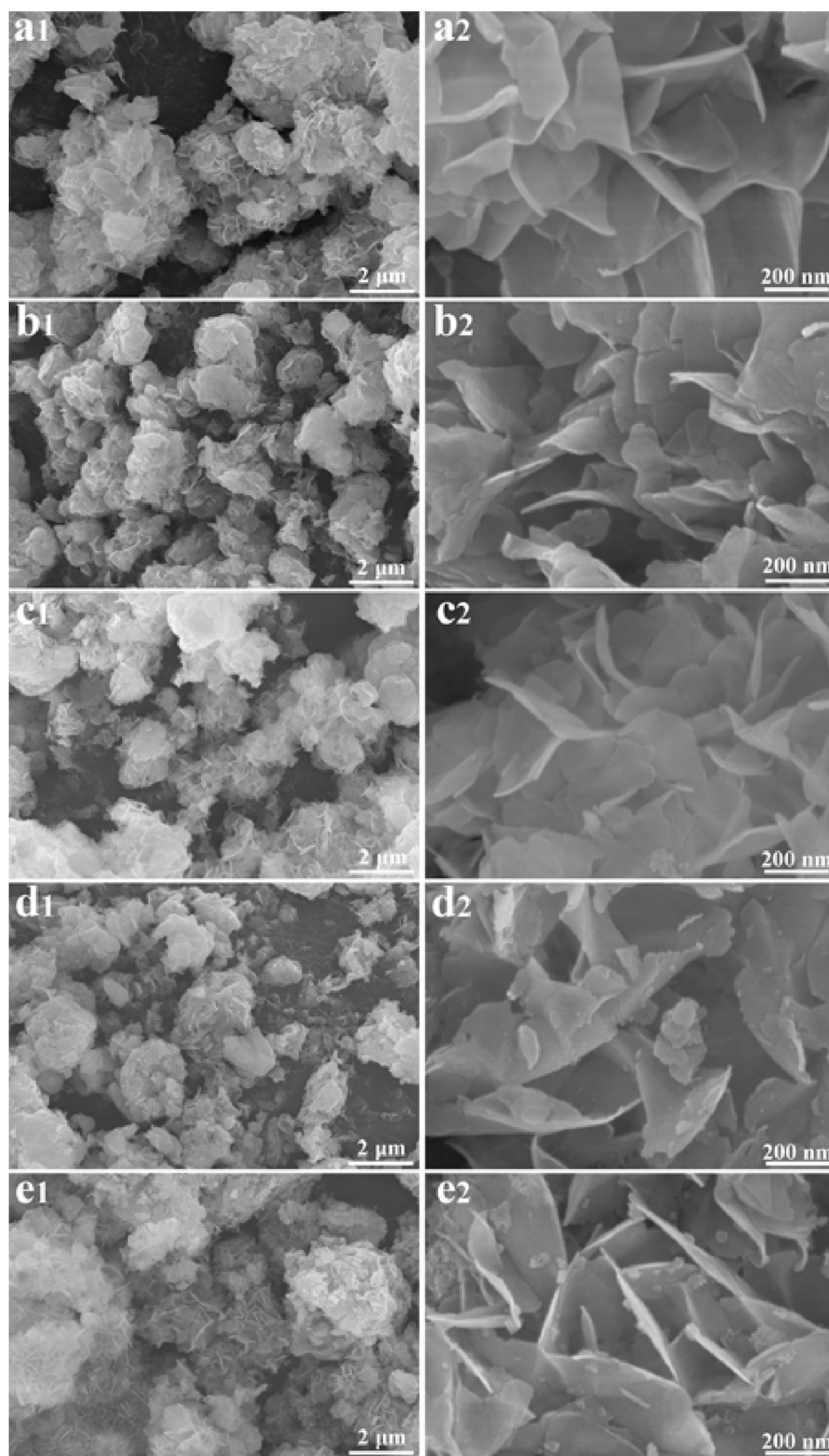
Fig. 6. SEM images of MIC samples: a1) Low and a2) high magnification SEM images of sample MnS/In$_2$S$_3$; b1) Low and b2) high magnification SEM images of MIC0.6; c1) Low and c2) high magnifcation SEM images of MIC1.2; d1) Low and d2) high magnification SEM images of MIC1.8; (e1) Low and e2) high magnification SEM images MIC3.0.
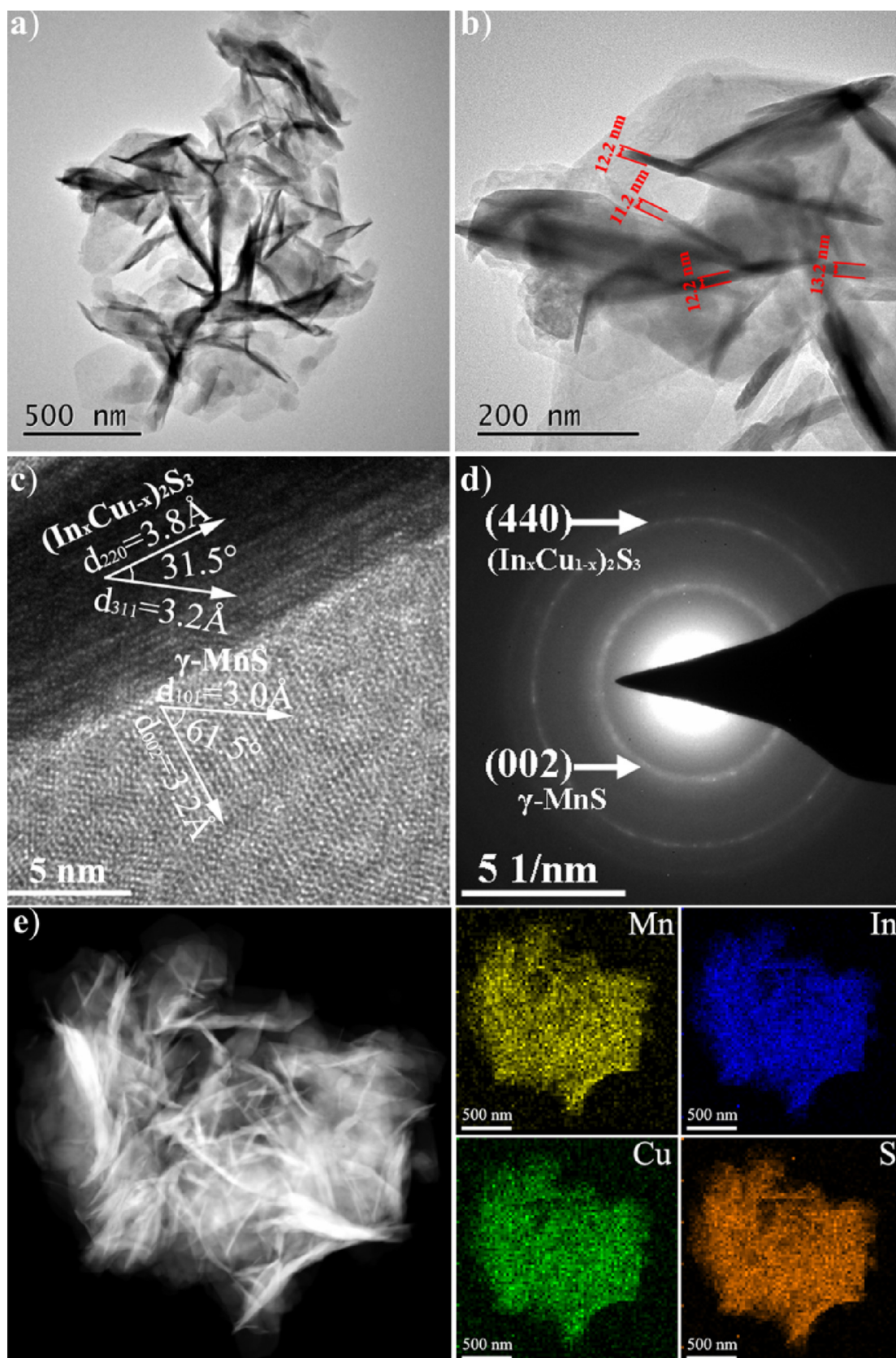
Fig. 7. a) Low- and b) high-magnification TEM images; c) HRTEM image; d) SAED pattern; e) EDX elemental mapping of the MIC1.2 sample.
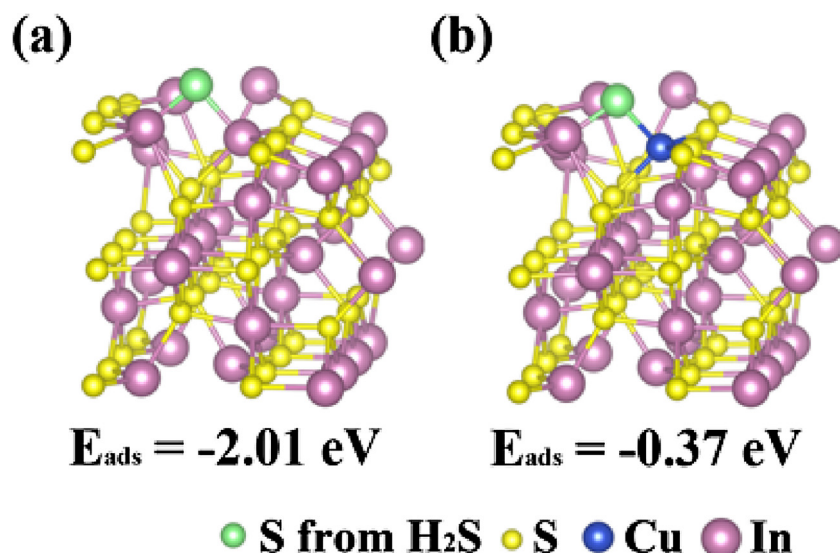
Fig. 8. The structures of S adsorbed on the surface of (a) β-In$_2$S$_3$ and (b) Cu-In$_2$S$_3$.

These results clearly revealed that S desorbs much easier from the surface of Cu-In$_2$S$_3$ than from In$_2$S$_3$. Hence, the existence of Cu could promote S desorption from the surface of β-In$_2$S$_3$ and avoid S occupying surface active sites, which plays an important role for long-term photocatalytic H$_2$ production from H$_2$S (cf. Fig. 1c). The case has been further verified by the XRD and XPS measurement results of the MnS/(In$_x$Cu$_{1-x}$)$_2$S$_3$ composite after the photocatalytic H$_2$ evolution reaction, as shown in Fig. S1. The phenomenon of sulfur deposition on the catalyst surface is not observed [12,17,18]. Therefore, the formation of (In$_x$Cu$_{1-x}$)$_2$S$_3$ solid solution is highly important to boost photocatalytic H$_2$ production because the excellent solar light capture and effective S desorption on the surface was simultaneously realized.

Finally, the (In$_x$Cu$_{1-x}$)$_2$S$_3$ solid solution is in close contact with γ-MnS nanosheets to from 2D layered heterostructures, which is believed to enhance the transfer of photo-generated electrons and holes at the interface and supresses their recombination as observed in Fig. 3.

4. Conclusion

In summary, we designed and reported a highly active noble-metal free MnS/(In$_x$Cu$_{1-x}$)$_2$S$_3$ composite based on the synergy of solid solution and heterojunctions. The maximum H$_2$ production rate of 29,252 μmol h^{-1} g^{-1} is achieved over the optimized MnS/(In$_x$Cu$_{1-x}$)$_2$S$_3$ composite under visible-light irradiation (λ > 420 nm), which is ca. 2.5 times higher than that of the pristine MnS/In$_2$S$_3$ (11,945 μmol h^{-1} g^{-1}) and 1400 times higher than that over CuS (21 μmol h^{-1} g^{-1}) alone. The corresponding AQE at 420 and 450 nm is 65.2% and 62.6%, respectively, which are the highest so far for the visible light photocatalytic splitting of H$_2$S in the absence of noble-metal co-catalysts. In combination with the experimental results and DFT calculation, we revealed that the addition of Cu prefers to form (In$_x$Cu$_{1-x}$)$_2$S$_3$ solid solution instead of Mn$_x$Cu$_{1-x}$S, which can simultaneously achieve the excellent solar light capture and effective S desorption on the catalyst surface. Moreover, the formed heterostructure between (In$_x$Cu$_{1-x}$)$_2$S$_3$ and γ-MnS can further promote the transfer of photo-generated electrons and holes, and suppresses their recombination. This study does not only report a highly active non-noble metal photocatalyst but also provides a novel "Solid solution-Heterojunction" strategy for boost photocatalytic H$_2$ production from a highly toxic pollutant.

Appendix A. Supplementary data

Supplementary material related to this article can be found, in the online version, at doi:https://doi.org/10.1016/j.apcatb.2018.11.016.

References

[1] A.P. Reverberi, J.J. Klemeš, P.S. Varbanov, B. Fabiano, J. Clean. Prod. 136 (2016) 72–80.
[2] X. Zhang, Y. Tang, S. Qu, J. Da, Z. Hao, ACS Catal. 5 (2015) 1053–1067.
[3] S.Z. Baykara, E.H. Figen, A. Kale, T. Nejat Veziroglu, Int. J. Hydrogen Energy 32 (2007) 1246–1250.
[4] V. Vorontsov, J.L. Luo, A.R. Sanger, K.T. Chuang, J. Power Sources 183 (2008) 76–83.
[5] A. Piéplu, O. Saur, J.C. Lavalley, O. Legendre, C. Nédez, Catal. Rev. 40 (1998) 409–450.
[6] J.S. Eow, Environ. Prog. Sustain. 21 (2002) 143–162.
[7] W. Xiao, P. Liu, J. Zhang, W. Song, Y.P. Feng, D. Gao, J. Ding, Adv. Energy Mater. 7 (2017) 1602086.
[8] X. Wu, H. Zhang, J. Dong, M. Qiu, J. Kong, Y. Zhang, Y. Li, G. Xu, J. Zhang, J. Ye, Nano Energy 45 (2018) 109–117.
[9] J. Liu, D. Zhu, T. Ling, A. Vasileff, S.Z. Qiao, Nano Energy 40 (2017) 264–273.
[10] L. Shang, B. Tong, H. Yu, G.I. Waterhouse, C. Zhou, Y. Zhao, M. Tahir, L.Z. Wu, C.H. Tung, T. Zhang, Adv. Energy Mater. 6 (2016) 1501241.
[11] B.B. Kale, J.O. Baeg, S.M. Lee, H. Chang, S.J. Moon, C.W. Lee, Adv. Funct. Mater. 16 (2006) 1349–1354.
[12] G. Ma, H. Yan, J. Shi, X. Zong, Z. Lei, C. Li, J. Catal. 260 (2008) 134–140.
[13] J.S. Jang, H. Gyu Kim, P.H. Borse, J.S. Lee, Int. J. Hydrogen Energy 32 (2007) 4786–4791.
[14] F. Wang, S. Wei, Z. Zhang, G.R. Patzke, Y. Zhou, Phys. Chem. Chem. Phys. 18 (2016) 6706–6712.
[15] R. Zhang, W. Wan, L. Qiu, Y. Wang, Y. Zhou, Appl. Surf. Sci. 419 (2017) 342–347.
[16] M. Shelef, K. Otto, N.C. Otto, Adv. Catal. 27 (1979) 311–365.
[17] M. Dan, Q. Zhang, S. Yu, A. Prakash, Y. Lin, Y. Zhou, Appl. Catal. B Environ. 217 (2017) 530–539.
[18] A. Prakash, M. Dan, S. Yu, S. Wei, Y. Li, F. Wang, Y. Zhou, Sol. Energy Mater. Sol. Cells 180 (2018) 205–212.
[19] Z. Li, Q. Zhang, M. Dan, Z. Guo, Y. Zhou, Mater. Lett. 201 (2017) 118–121.
[20] M. Dan, Q. Zhang, Y. Zhong, Y. Zhou, J. Inorg. Mater. 32 (2017) 1308–1314.
[21] Z. Li, Z. Zhou, J. Ma, Y. Li, W. Peng, G. Zhang, F. Zhang, X. Fan, Appl. Catal. B Environ. 237 (2018) 288–294.

[22] H. Wang, L. Zhang, Z. Chen, J. Hu, S. Li, Z. Wang, J. Liu, X. Wang, Chem. Soc. Rev. 43 (2014) 5234–5244.
[23] Y. Zhong, G. Zhao, F. Ma, Y. Wu, X. Hao, Appl. Catal. B Environ. 199 (2016) 466–472.
[24] W. Wan, R. Zhang, M. Ma, Y. Zhou, J. Mater. Chem. A 6 (2018) 754–775.
[25] W. Jiang, Y. Liu, R. Zong, Z. Li, W. Yao, Y. Zhu, J. Mater. Chem. A 3 (2015) 18406–18412.
[26] J.Y. Do, R.K. Chava, S.K. Kim, K. Nahm, N.K. Park, J.P. Hong, S.J. Lee, M. Kang, Appl. Surf. Sci. 451 (2018) 86–98.
[27] H. Zhang, Y. Zhu, J. Phys. Chem. C 114 (2010) 5822–5826.
[28] I. Tsuji, H. Kato, A. Kudo, Angew. Chem. Int. Ed. 44 (2005) 3565–3568.
[29] I. Tsuji, H. Kato, A. Kudo, Chem. Mater. 18 (2006) 1969–1975.
[30] I. Tsuji, H. Kato, H. Kobayashi, A. Kudo, J. Phys. Chem. B 109 (2005) 7323–7329.
[31] T. Kato, Y. Hakari, S. Ikeda, Q. Jia, A. Iwase, A. Kudo, J. Phys. Chem. Lett. 6 (2015) 1042–1047.
[32] S. Brunauer, P.H. Emmett, E. Teller, J. Am. Chem. Soc. 60 (1938) 309–319.
[33] A. Zimina, K. Dardenne, M.A. Denecke, D.E. Doronkin, E. Huttel, H. Lichtenberg, S. Mangold, T. Pruessmann, J. Rothe, Th. Spangenberg, R. Steininger, T. Vitova, H. Geckeis, J.-D. Grunwaldt, Rev. Sci. Instrum. 88 (2017) 113113.
[34] B. Ravel, M. Newville, J. Synchrotron Radiat. 12 (2005) 537–541.
[35] J.J. Rehr, J.J. Kas, F.D. Vila, M.P. Prange, K. Jorissen, Phys. Chem. Chem. Phys. 12 (2010) 5503–5513.
[36] J.P. Perdew, K. Burke, M. Ernzerhof, Phys. Rev. Lett. 77 (1996) 3865–3868.

[37] G. Kresse, J. Furthermuller, Phys. Rev. B 54 (1996) 11169.
[38] K. Chang, X. Hai, J. Ye, Adv. Energy Mater. 6 (2016) 1502555.
[39] X. Chen, L. Li, W. Zhang, Y. Li, Q. Song, L. Dong, ACS Sustain. Chem. Eng. 4 (2016) 6680–6688.
[40] J. Ran, J. Zhang, J. Yu, M. Jaroniec, S.Z. Qiao, Chem. Soc. Rev. 43 (2014) 7787–7812.
[41] J. Zhang, J. Yu, Y. Zhang, Q. Li, J.R. Gong, Nano Lett. 11 (2011) 4774–4779.
[42] M. Liu, L. Zhang, X. He, B. Zhang, H. Song, S. Li, W. You, J. Mater. Chem. A 2 (2014) 4619–4626.
[43] Y. Li, G. Chen, Q. Wang, X. Wang, A. Zhou, Z. Shen, Adv. Funct. Mater. 20 (2010) 3390–3398.
[44] L. An, L. Huang, P. Zhou, J. Yin, H. Liu, P. Xi, Adv. Funct. Mater. 25 (2015) 6814–6822.
[45] K.A. Cychosz, R. Guillet-Nicolas, J. Garcia-Martinez, M. Thommes, Chem. Soc. Rev. 46 (2017) 389–414.
[46] J.S. Hu, L.L. Ren, Y.G. Guo, H.P. Liang, A.M. Cao, L.J. Wan, C.L. Bai, Angew. Chem. Int. Ed. 117 (2005) 1295–1299.
[47] X. Li, J. Yu, M. Jaroniec, Chem. Soc. Rev. 45 (2016) 2603–2636.
[48] T. Kako, H. Irie, K. Hashimoto, J. Photochem. Photobiol. A: Chem. 171 (2005) 131–135.
[49] S. Kataoka, E. Lee, M.I. Tejedor-Tejedor, M.A. Anderson, Appl. Catal. B Environ. 61 (2005) 159–163.
[50] N. Bühler, K. Meier, J.-F. Reber, J. Phys. Chem. 88 (1984) 3261–3268.